applied sciences

MDPI

Article

Research on Inertial Force Attenuation Structure and Semi-Active Control of Regenerative Suspension

Huixin Song [1,2], Mingming Dong [1,*] and Xin Wang [3]

[1] School of Mechanical Engineering, Beijing Institute of Technology, Beijing 100081, China; songhuixinlw@163.com
[2] Basic and Frontier Technology Department, China North Vehicle Research Institute, Beijing 100072, China
[3] School of Vehicle and Mobility, Tsinghua University, Beijing 100084, China; wangxin1991@mail.tsinghua.edu.cn
* Correspondence: vdmm@bit.edu.cn

Abstract: To improve the energy recovery ability of the energy-regenerative suspension, a transmission is generally used to increase the motor speed, but this results in a significant increase in the equivalent inertial mass of the suspension. The research on energy-regenerative suspension has been ongoing for more than 20 years, but there have been few product applications, mainly due to the failure to solve the problem of the deterioration of suspension performance caused by equivalent inertial mass. This paper proposes a new suspension configuration with the suspension shock absorber connected to a high-frequency vibration reduction structure and establishes a vibration transmission model. Through frequency domain analysis, it has been conclusively proven that the new-configuration can significantly reduce both the sprung mass acceleration and relative dynamic load of the energy regenerative suspension. On the basis of frequency domain analysis, a scheme based on PWM control of the dissipation resistance value of the energy regenerative suspension is proposed, and through bench comparison experiments, it has been verified that the new-configuration suspension can eliminate the oscillation of the damping force curve of the shock absorber and significantly improve the suspension performance. Further experiments show that using the skyhook semi-active control algorithm the new-configuration suspension can further reduce the sprung mass acceleration and relative dynamic load.

Keywords: inertial force; regenerative suspension; semi-active control; suspension configuration

check for updates

Citation: Song, H.; Dong, M.; Wang, X. Research on Inertial Force Attenuation Structure and Semi-Active Control of Regenerative Suspension. *Appl. Sci.* **2024**, *14*, 2314. https://doi.org/10.3390/app14062314

Academic Editors: Marco Troncossi and Nicola Bosso

Received: 16 February 2024
Revised: 5 March 2024
Accepted: 7 March 2024
Published: 9 March 2024

1. Introduction

With the advancement of new-energy vehicle technology, the pursuit of enhanced energy utilization efficiency has led to a growing focus on regenerative suspensions capable of energy recovery. Karnopp [1] proposed the working principle of a linear regenerative damper in 1989, which uses the vertical displacement of the damper to drive the coil to cut the magnetic induction line, generating electrical energy under the action of electromagnetic induction. In 2004, BOSE Company successfully developed a linear-motor-based regenerative suspension [2]. When working in the energy feedback state, the electromagnetic damping force can be adjusted to adapt to different road conditions. During acceleration, braking, or steering processes, the body can be controlled for anti-pitch and anti-roll. In terms of energy recovery research on regenerative suspension, X. Zheng et al. [3] proposed a regenerative shock absorber based on ball-screw transmission, which can achieve switching between two modes. Q. Xiong [4] proposed a rule-based control strategy for a mechanical motion-rectifier regenerative damper, which improved performance by 29.2% compared to traditional dampers and achieved an average power of 187 W. Z. Gao [5] analyzed the process of energy flow transmission, dissipation, and recovery within the suspension system, and studied the energy flow mechanisms of different control strategies for suspension. The proposed control strategy combines ride comfort and energy recovery efficiency and has obvious advantages over traditional control strategies. The system energy consumption is reduced by at least 14.51%, and an additional 2.45% of energy is recovered. X. Tang et al. [6] from New York University conducted relevant research on linear-motor-type regenerative dampers and manufactured a 1:2 scaled prototype based on a theoretical model. The experimental results showed that the system can achieve a feed power of 16–64 W under the excitation of the root mean square velocity of 0.25–0.5 m/s. The linear shock absorber developed by Lee J et al. [7] has a maximum power and an average power of 250 W and 100 W, respectively. The regenerative suspension proposed by S. Li et al. [8] can recover energy from vehicle vibration for storage in batteries, increasing efficiency by 35.24%, and the damping coefficient can also be accurately adjusted in real time. Y. Hua et al. [9] developed a regenerative damper for high-speed trains, which uses ball-screw transmission to achieve energy recovery of 25.89–153.19 W. Abdelkareem M. A. A. et al.'s [10] research shows that a harvested average power of 350 W could be achieved for a medium-size sedan, and a wide range of the harvestable power over 1 kW could be achieved for heavy-duty and off-road vehicles.

However, equivalent inertial mass has a significant impact on suspension performance and reliability [11] and has become a challenge for the commercialization of regenerative suspension products. During the vertical reciprocating motion of the suspension, rotating components with a moment of inertia generate inertial forces. If the rotational acceleration is too large, rotating components will generate excessive impact torque, causing damage to weaker components such as the transmission device and connecting shaft. On the other hand, this part of the impact torque will have a very adverse impact on suspension performance.

The suspension motion is translational, and the inertial mass hinders the suspension motion. The rotating parts of the transmission, motor, and other parts of the energy regenerative suspension have the moment of inertia, which hinders the rotating movement of the motor and other parts. For the convenience of research, the moment of inertia of the rotating parts of the shock absorber is converted into the equivalent inertial mass of the suspension translation. The greater the equivalent inertial mass is, the greater the inertial force will be generated under the random excitation of the road surface, which will cause the suspension performance to deteriorate.

Many scholars have recognized the adverse effects of equivalent inertial mass on suspension. Z. Li et al. [12] developed a recoverable energy shock absorber, calculated the equivalent inertial mass, and experimentally proved that the equivalent inertial mass causes significant fluctuations in the damping force curve of the shock absorber. S. Liu [13] and H. Peng [14] showed that equivalent inertial mass improves the performance of the suspension in the low-frequency region, while it deteriorates in the high-frequency region.

To reduce the impact of equivalent inertial mass, the reciprocating motion of the motor is generally converted into unidirectional motion. C. Yu et al. [15] optimized the unidirectional rotation and asymmetric damping characteristics of the motor by combining two unidirectional clutches and planetary gear mechanisms. Z. Wang et al. [16] developed a double-screw rotary motor linear shock absorber with a one-way clutch. L. Hai [17] developed a rotary-motor-type linear shock absorber with a dual tooth gear rack and a one-way clutch. L. Dong [18] developed a rotary-motor-type linear shock absorber with three bevel gears and two one-way clutches. A one-way clutch can reduce the impact during reversing, but it cannot solve the impact problem during acceleration or deceleration in the same direction. For this reason, Z. Zhao et al. [19] proposed an added-vibration-reduction structure (AVRS) between the wheel and the regenerative shock absorber, as shown in Figure 1a, and research has shown that AVRS significantly reduces the impact of equivalent inertial mass, making suspension performance close to ideal performance. Montazeri et al. [20] proposed a scheme of regenerative shock absorber with series spring, as shown in Figure 1b, and the study showed that the spring stiffness should be larger than the suspension stiffness, and the spring in series makes the regenerative damper free from equivalent inertial mass interference at high frequency, which is beneficial for the performance improvement of the regenerative suspension. Chen Shian et al. [21] proposed a dual vibration reduction structure (DVRS) with an additional spring and damper in series throughout the regenerative suspension to reduce the effect of equivalent inertial mass, as shown in Figure 1c.

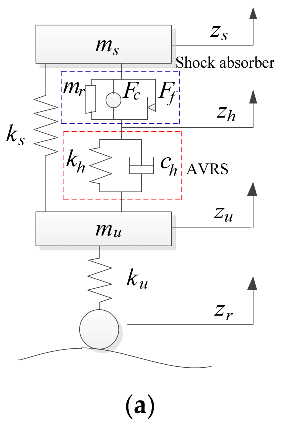

Figure 1. (**a**) Added vibration reduction structure (AVRS); (**b**) series spring vibration reduction structure; (**c**) dual vibration reduction structure (DVRS).

We have reviewed the measures taken to improve the performance of traditional suspensions and compared them with the measures taken to improve the performance of energy regenerative suspensions. We found that the commonality is to improve the high-frequency performance of suspensions. In the 1950s, in order to solve the problem of delayed oil filling of shock absorbers, pneumatic hydraulic shock absorbers [22,23] were developed, such as the monotube pneumatic shock absorber with its cylinder filled with nitrogen [24], which helps to eliminate idle travel, prevent oil emulsification, avoid distortion of the damping characteristics, effectively eliminate high-frequency vibration and noise, improve the grounding of tires, and improve the comfort of the ride [25]. The air chamber in series with the damping valve in the inflatable hydraulic damper acts as a low-pass filter.

In order to improve the suspension performance, some studies have proposed the structure of a conventional suspension damper with series springs. Mikułowski G et al. [26] and Martini A et al. [27] connected the damper in series with oil and gas springs to reduce the dynamic wheel loads and keep the comfort of the vehicle unchanged. Chen Jie et al. [28] improved the vibration absorber of the vehicle body by connecting the shock absorber in the original vibration absorber with the spring in series, forming a ternary vibration absorber composed of two springs and one shock absorber. Much research has shown that the new structure reduces the root mean square value of the vehicle body vibration acceleration and effectively reduces the elastic vibration of the vehicle body.

To solve the problem of excessive inertial force in the high-frequency region of the energy-regenerative suspension, this paper proposes a high-frequency vibration reduction structure (HVRS) scheme that connects the shock absorber and unsprung mass in series. Through the low-pass filtering effect of the elastic components in the HVRS, the energy-regenerative shock absorber aims to enhance its strengths and avoid its weaknesses, meeting the demand for large damping in the low-frequency region. At the same time, it reduces the adverse effects of inertial and damping forces in the high-frequency region on the root mean square value of sprung mass acceleration.

This paper establishes a dynamic model of the original configuration of energy-regenerative suspension and analyzes the adverse effect of equivalent inertial mass on suspension characteristics. To solve the problem caused by equivalent inertial mass, a scheme of connecting the HVRS with the energy regenerative shock absorber is proposed. Through frequency domain comparative analysis, it is proved that the HVRS is beneficial for reducing the acceleration of sprung mass and relative dynamic load, thereby improving the driving comfort and handling of vehicles. To further verify the role of the HVRS, its implementation form is analyzed and applied to the improvement of existing energy regenerative suspension. Through PWM control, the suspension controller can achieve linear adjustment of the dissipation resistance value of the energy-regenerative suspension. Through bench test comparison, it is proven that HVRS energy-regenerative suspension can solve the problem of equivalent inertial mass. Further verification demonstrates that the application of the skyhook control algorithm can further improve suspension performance.

2. The Structure and Working Principle of Energy-Regenerative Shock Absorbers

The structural principle of the energy-regenerative suspension damper used in this article is shown in Figure 2a. The actuator consists of a gear rack, a box, a planetary reducer, an electric motor, an upper mounting seat, a cylinder, a lower mounting seat, etc. The prototype of the shock absorber is shown in Figure 2b.

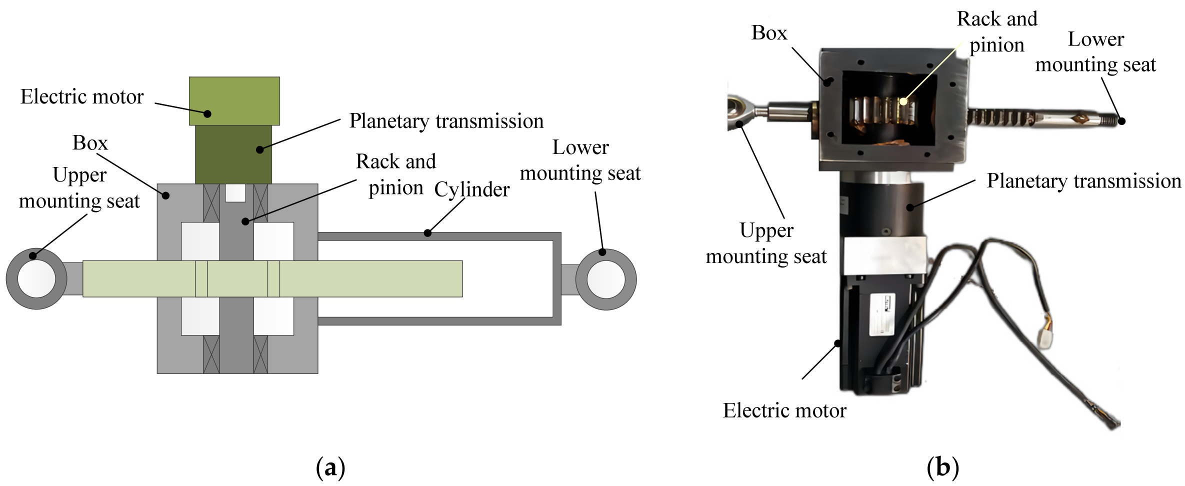

Figure 2. (**a**) Structural principle of shock absorber; (**b**) shock absorber prototype.

In application, the energy-regenerative shock absorber in Figure 2 is connected in parallel with the steel coil spring to form an energy-regenerative suspension. The configuration and working principle of the energy-regenerative suspension are shown in Figure 3. During vehicle operation, the road surface stimulates the vertical movement of the wheels. The vertical motion of the wheels is transmitted to the motor through the rack and pinion and planetary transmission, which is dragged to convert the mechanical energy of suspension vibration into electrical energy. The alternating current generated by the motor enters the three-phase rectifier bridge through the three-phase windings ua, ub, and uc of the motor, and becomes a direct current after rectification. The electrical energy of the motor ultimately enters the energy-consuming or absorbing module. In the energy-consuming or absorbing module, Dr and Dp are electronic switches, Rr is a resistor, Cr is the consuming mode control line, and Cp is the absorbing mode control line.

The suspension controller can achieve two control modes of energy-regenerative suspension, namely energy-consuming mode and energy-absorbing mode. In energy-consuming mode, the suspension controller controls the electronic switch Dr to adjust the power consumption of the resistor Rr, forming the electromagnetic force that hinders the relative movement of the wheel and the sprung mass.

In energy-absorbing mode, the suspension controller controls the electronic switch Dp to regulate the ability to absorb electrical energy, forming the electromagnetic force that hinders the relative movement of the wheel and the sprung mass. The electrical energy is stabilized within the range that the battery can charge through the voltage stabilization module, and finally, the electrical energy is charged into the battery, achieving the absorption of suspension vibration energy.

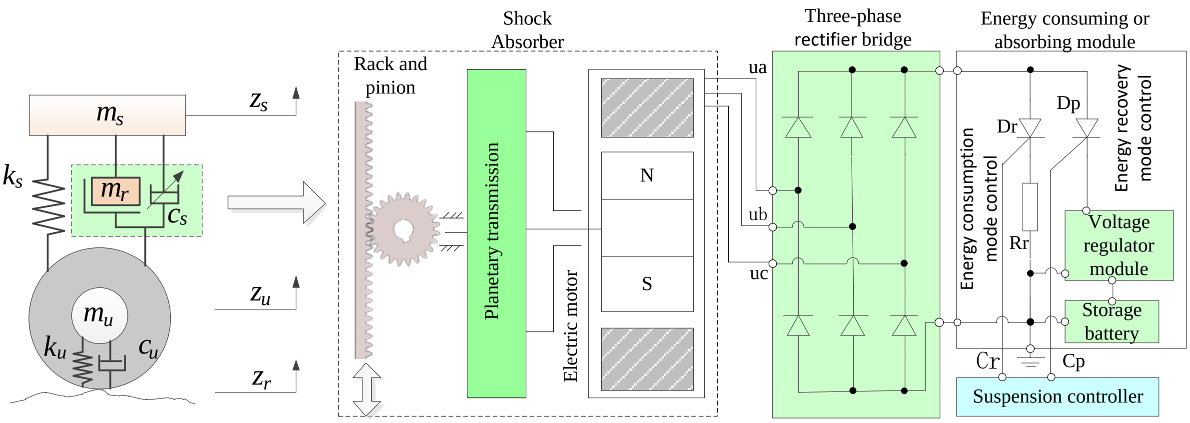

Figure 3. The configuration of energy-regenerative suspension.

The symbols in the configuration are defined as follows: m_s is sprung mass, m_u is unsprung mass, m_r is equivalent inertial mass, k_s is suspension spring stiffness, k_u is wheel stiffness, c_s is suspension damping coefficient, c_u is wheel damping coefficient, z_s is sprung mass displacement, z_u is unsprung mass displacement, z_r is road excitation displacement.

The moment of inertia J in a rotational inertial frame is similar to the inertial mass m in a translational inertial frame, both of which hinder the motion of an object. Inertial mass m hinders the translational motion of an object, while the moment of inertia J hinders the rotational motion of an object. To facilitate the analysis of the performance of the energy-regenerative suspension, it is necessary to convert the moment of inertia J in the shock absorber into an inertial mass m. For a rotation radius of r, the moment of inertia with uniform mass distribution is J, the relationship between the moment of inertia J and the equivalent inertial mass m_r in a translational inertial frame is Equation (1):

$$m_r = J/r^2 \tag{1}$$

To better convert the mechanical energy of suspension vibration into electrical energy, it is necessary to increase the speed of the motor as much as possible so that the electromagnetic damping force is sufficiently large. In order to improve the speed of the motor, this study applies rack and pinion to convert the vertical motion of the wheel relative to the sprung mass into rotational motion and further amplifies the rotational motion through a planetary transmission. Although the growth rate has been achieved, the equivalent inertial mass m_r, brought about by the energy regenerative suspension and during the suspension motion process, will produce inertial force F_r. The magnitude of inertial force is related to the acceleration a_r of the suspension motion, and the calculation formula is shown in Equation (2). Therefore, the inertial force generated by the equivalent inertial mass will have an impact on the motion of the wheel and the sprung mass.

$$F_r = m_r a_r \tag{2}$$

The parameters of the shock absorber are shown in Table 1. According to the parameters in Table 1, the equivalent inertial mass of the actuator can be calculated as shown in Equation (3).

$$m_r = (i_r^2 J_m + i_r^2 J_r + J_g)/r_g^2 = 58.8\text{kg} \tag{3}$$

Table 1. Parameters of rack and pinion shock absorber.

Parameter	Symbol	Value	Unit
Motor rated power	P_{me}	1000	W
Rated torque of motor	T_{me}	3.18	N·m
Motor speed	n_{me}	3000	r/min
Motor moment of inertia	J_m	0.000136	kg·m^2
Rated torque of planetary transmission	T_{re}	130	N·m
Rated speed of planetary transmission	n_{re}	3000	r/min
Rotational inertia of planetary transmission	J_r	0.00005	kg·m^2
Planetary transmission ratio	i_r	16	
Gear indexing circle radius	r_g	0.0285	m
Gear rotational inertia	J_g	0.00013	kg·m^2

3. Frequency Domain and the Time Domain Characteristics of Traditional Configuration Energy Feedback Suspension

According to the traditional configuration, the dynamic equation of the suspension system is obtained as shown in Equation (4).

$$\begin{cases} m_s\ddot{z}_s = k_s(z_u - z_s) + c_s(\dot{z}_u - \dot{z}_s) + m_r(\ddot{z}_u - \ddot{z}_s) \\ m_u\ddot{z}_u = k_s(z_s - z_u) + k_u(z_r - z_u) + c_s(\dot{z}_s - \dot{z}_u) + c_u(\dot{z}_r - \dot{z}_u) + m_r(\ddot{z}_s - \ddot{z}_u) \end{cases} \tag{4}$$

The static load of the wheels when the suspension system is balanced is G_j; the dynamic load on the wheels during the suspension system movement is F_d. By performing Fourier transform on Equation (4), $\ddot{z}_s = (\mathrm{j}\omega)^2 z_s$, $\dot{z}_s = \mathrm{j}\omega z_s$, $\ddot{z}_u = (\mathrm{j}\omega)^2 z_u$, $\dot{z}_u = \mathrm{j}\omega z_u$, the amplitude-frequency characteristics of the sprung mass acceleration $\ddot{z}_s$, relative dynamic load F_d/G_j, suspension dynamic deflection s_d, and equivalent inertial mass acceleration a_d relative to the road excitation speed $\dot{z}_r$ of the suspension can be obtained, as shown in Equations (5)–(9).

$$|H(\mathrm{j}\omega)|_{\ddot{z}_s \sim \dot{z}_r} = \omega\left|\frac{X_{z_s}}{X_{z_r}}\right| \tag{5}$$

$$|H(\mathrm{j}\omega)|_{(F_d/G_j)\sim\dot{Z}_r} = \frac{\omega_{s0}}{\omega(1+\mu)g}|\gamma\omega_{s0} + 2\varepsilon\xi\omega\mathrm{j}|\left|\frac{X_{F_d}}{X_{z_r}}\right| \tag{6}$$

$$|H(\mathrm{j}\omega)|_{s_d \sim \dot{z}_r} = \frac{1}{\omega}\left|\frac{X_{s_d}}{X_{z_r}}\right| \tag{7}$$

$$|H(\mathrm{j}\omega)|_{v_d \sim \dot{z}_r} = \left|\frac{X_{s_d}}{X_{z_r}}\right| \tag{8}$$

$$|H(\mathrm{j}\omega)|_{a_d \sim \dot{z}_r} = \omega\left|\frac{X_{s_d}}{X_{z_r}}\right| \tag{9}$$

$X_{z_s} = A_{su}A_r$; $X_{z_r} = A_sA_u - A_{su}^2$; $X_{F_d} = A_sA_u - A_{su}^2 - A_sA_r$; $X_{s_d} = (A_{su} - A_s)A_r$;
$A_s = 1 - (1+\mu\beta)\lambda^2 + 2\mathrm{j}\xi\lambda$; $A_{su} = 1 - \mu\beta\lambda^2 + 2\mathrm{j}\xi\lambda$;
$A_u = 1 + \gamma - \mu\lambda^2 - \mu\beta\lambda^2 + 2\mathrm{j}\xi\lambda + 2\mathrm{j}\varepsilon\xi\lambda$; $A_r = \gamma + 2\mathrm{j}\varepsilon\xi\lambda$.

The ratio of the wheel damping coefficient to the suspension damping coefficient is $\varepsilon = c_u/c_s$. The ratio of wheel stiffness coefficient to suspension stiffness coefficient $\gamma = k_u/k_s$. Unsprung mass to sprung mass ratio $\mu = m_u/m_s$. The equivalent inertial mass to unsprung mass ratio $\beta = m_r/m_u$. Suspension damping ratio $\xi = c_s/2\sqrt{k_s m_s}$.

f_{s0} is the bias frequency of the sprung mass when the equivalent inertial mass is zero: $f_{s0} = (\sqrt{k_s/m_s})/2\pi$. f_{ss} is the bias frequency of the sprung mass when considering the equivalent inertial mass: $f_{ss} = \sqrt{k_s/(m_s + m_r)}/(2\pi)$. f_{u0} is the bias frequency of the unsprung mass when considering the equivalent inertial mass: $f_{u0} = \sqrt{(k_s + k_u)/m_u}/(2\pi)$. f_u is the bias frequency of the unsprung mass when considering the equivalent inertial mass:

$f_u = \sqrt{(k_s + k_u)/(m_u + m_r)}/(2\pi)$. is the frequency ratio; f is the excitation frequency of the road input, $\lambda = f/f_{s0}$.

The frequency domain characteristics of two suspension configurations are obtained. The simulation parameters are shown in Table 2. Equations (5)–(9) are calculated to obtain a comparison of the amplitude-frequency characteristics of the energy-regenerative suspension and the suspension with an equivalent inertial mass of 0 kg, as shown in Figure 4.

Table 2. Parameters of simulation.

Parameter	Value	Parameter	Value
ξ	0.25	μ	0.14
ε	0.043	γ	9
β	1.35		

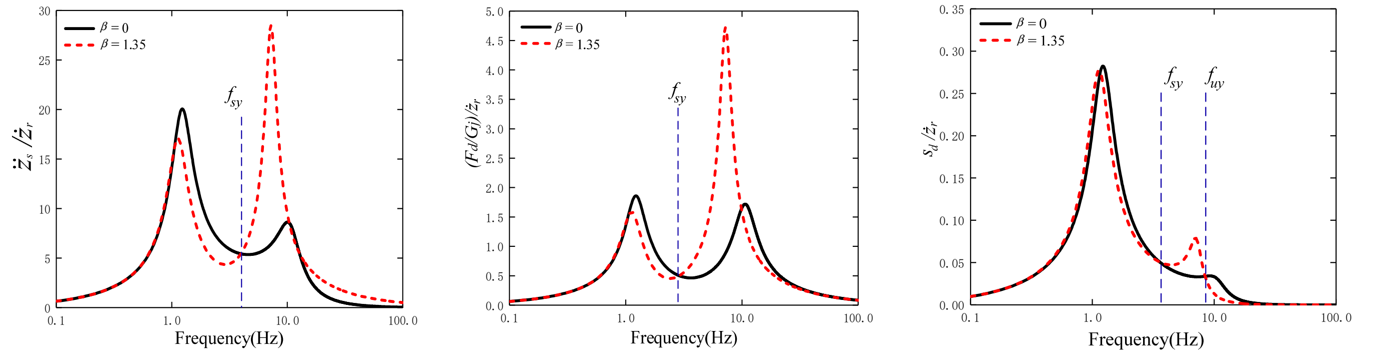

(**a**) (**b**) (**c**)

Figure 4. (**a**) Characteristics of sprung mass acceleration; (**b**) characteristics of relative dynamic load; (**c**) characteristics of suspension dynamic deflection.

In Figure 4a–c, the frequency of the intersection of suspension characteristic curves with different equivalent inertial masses on the right side of the first main frequency is f_{sy}. In Figure 4c, on the right side of the second main frequency of the suspension with an inertia mass ratio of 1.35, the intersection frequency of its dynamic deflection and the dynamic deflection of the suspension with an inertia mass ratio of 0 is f_{uy}.

From Figure 4a, it can be seen that when the excitation frequency is less than the frequency f_{sy}. The larger the equivalent inertial mass ratio, the smaller the acceleration value of the sprung mass. When the excitation frequency is higher than the frequency f_{sy}, the larger the equivalent inertial mass ratio, the greater the acceleration value of the spring-loaded mass. In the second frequency range, compared to the suspension without equivalent inertial mass, the equivalent inertial mass causes a significant increase in the acceleration of the sprung mass, which greatly affects the comfort of vehicle driving.

From Figure 4b, it can be seen that when the excitation frequency f is less than the frequency f_{sy}, the amplitude of the relative dynamic load decreases with the increase of the equivalent inertial mass ratio. When the excitation frequency f is greater than the frequency f_{sy}, the larger the equivalent inertial mass ratio, the greater the relative dynamic load. In the second frequency range, compared to the suspension without equivalent inertial mass, the equivalent inertial mass causes a significant increase in relative dynamic load, which greatly affects the vehicle's handling stability.

From Figure 4c, it can be seen that when the excitation frequency f is less than the frequency, the amplitude of the suspension dynamic deflection decreases with the increase of the equivalent inertial mass ratio. When the excitation frequency f is greater than the frequency but less than the frequency f_{uy}, the equivalent inertial mass causes a significant increase in relative dynamic deflection. When the excitation frequency f is greater than the frequency f_{uy}, the equivalent inertial mass reduces the relative dynamic deflection.

From the above analysis, it can be seen that the main problem of energy-regenerative suspension is how to reduce the adverse effects of equivalent inertial mass above the frequency f_{sy} band, and improve the driving comfort and handling stability of the vehicle.

4. The Improved Configuration of Energy Regenerative Suspension

4.1. Improved Two-Degree-of-Freedom Energy-Regenerative Suspension Mathematical Model

The improved energy-regenerative suspension is shown in Figure 5. The improved suspension configuration adds a high-frequency vibration reduction structure (HVRS) between the regenerative shock absorber and the wheel to reduce the impact of equivalent inertial mass.

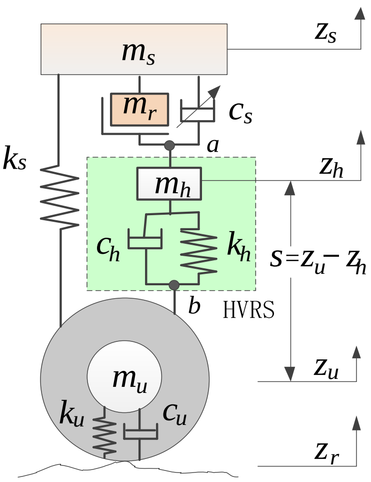

Figure 5. Energy-regenerative suspension configuration with HVRS.

In Figure 5, m_h represents the mass of the HVRS, k_h represents the stiffness coefficient of the HVRS, c_h represents the damping coefficient of the HVRS, and z_h represents the displacement of the HVRS. The ratio of the HVRS damping coefficient to the wheel damping coefficient is χ = ch/cu; the ratio of HVRS stiffness to suspension stiffness is $\delta = k_h/k_s$; the ratio of HVRS mass to unsprung mass is $\varsigma = m_h/m_u$.

According to Figure 5, when the deformation s of the HVRS is less than its stroke L_h, the HVRS takes effect. The dynamic equation of a suspension with an HVRS with two degrees of freedom is established as Equation (10). When the deformation s of the HVRS is greater than or equal to its stroke L_h, the HVRS is not effective. Assuming no impact occurs when the HVRS is stretched or compressed to the end of its stroke, the new suspension configuration has the same characteristics as the traditional suspension configuration, and its suspension motion is shown in Equation (4).

$$\begin{cases} m_s\ddot{z}_s = k_s(z_u - z_s) + c_s(\dot{z}_h - \dot{z}_s) + m_r(\ddot{z}_h - \ddot{z}_s) \\ m_h\ddot{z}_h = k_h(z_u - z_h) + c_h(\dot{z}_u - \dot{z}_h) - m_r(\ddot{z}_h - \ddot{z}_s) - c_s(\dot{z}_h - \dot{z}_s) \\ m_u\ddot{z}_u = k_s(z_s - z_u) + k_u(z_r - z_u) + k_h(z_h - z_u) + c_u(\dot{z}_r - \dot{z}_u) + c_h(\dot{z}_h - \dot{z}_u) \end{cases} \tag{10}$$

By performing the Fourier transform on Equation (10), the amplitude-frequency characteristics of the sprung mass acceleration $\ddot{z}_s$, relative dynamic load F_d/G_j, suspension dynamic deflection s_d, shock absorber velocity v_{sh}, and HVRS shock absorber velocity v_{hu}, equivalent inertial mass acceleration a_{hu} relative to the road excitation velocity $\dot{z}_r$ can be obtained, as shown in Equations (11)–(16).

$$|H_h(\mathrm{j}\omega)|_{\ddot{z}_s\sim\dot{z}_r} = \left|\frac{\ddot{z}_s}{\dot{z}_r}\right| = \omega\left|\frac{X_{z_{sh}}}{X_{z_{rh}}}\right| \tag{11}$$

$$\left|H_h(\mathrm{j}\omega)_{(F_d/G_j)\sim\dot{Z}_r}\right| = \left|\frac{k_u(z_r - z_u) + c_u(\dot{z}_r - \dot{z}_u)}{(m_s + m_u)g}\right| = \left|\frac{\omega_{s0}(\gamma\omega_{s0} + 2\varepsilon\xi\omega\mathrm{j})}{(1+\mu)g}\right|\left|\frac{X_{F_{dh}}}{X_{z_{rh}}}\right| \tag{12}$$

$$|H_h(\mathrm{j}\omega)|_{s_d\sim\dot{z}_r} = \frac{1}{\omega}\left|\frac{X_{s_{dh}}}{X_{z_{rh}}}\right| \tag{13}$$

$$|H_h(\mathrm{j}\omega)|_{v_{sh}\sim\dot{z}_r} = \left|\frac{X_{v_{sh}}}{X_{z_{rh}}}\right| \tag{14}$$

$$|H_h(\mathrm{j}\omega)|_{a_{sh}\sim\dot{z}_r} = \omega\left|\frac{X_{v_{sh}}}{X_{z_{rh}}}\right| \tag{15}$$

$$|H_h(\mathrm{j}\omega)|_{v_{hu}\sim\dot{z}_r} = \left|\frac{X_{v_{hu}}}{X_{z_{rh}}}\right| \tag{16}$$

$X_{z_{sh}} = A_{hr}A_{hb} + A_{hr}A_{ha}A_{ua}$, $X_{z_{rh}} = A_{ub}A_{sa}A_{hb} - A_{ub}A_{ha}A_{sb} - A_{hb} - A_{ha}A_{ua} - A_{hc}A_{sb} - A_{hc}A_{sa}A_{ua}$,

$X_{F_{dh}} = X_{zrh} - A_{hr}A_{sa}A_{hb} + A_{hr}A_{ha}A_{sb}$, $X_{s_{dh}} = A_{hr}(A_{hb} + A_{ha}A_{ua}) - A_{hr}(A_{sa}A_{hb} - A_{ha}A_{sb})$,

$X_{v_{sh}} = A_{hr}(A_{hb} + A_{ha}A_{ua}) - A_{hr}(A_{sa}A_{ua} + A_{sb})$, $X_{v_{hu}} = A_{hr}(A_{sb} + A_{sa}A_{ua}) - A_{hr}(A_{sa}A_{hb} - A_{ha}A_{sb})$.

$A_{sa} = 1 - (1+\mu\beta)\lambda^2 + 2\xi\lambda\mathrm{j}$, $A_{ha} = -\mu\beta\lambda^2 + 2\xi\lambda\mathrm{j}$, $A_{sb} = -\mu\beta\lambda^2/\delta + 2\xi\lambda\mathrm{j}/\delta$, $A_{ua} = 1 + 2\chi\varepsilon\xi\lambda\mathrm{j}/\delta$,

$A_{hb} = 1 - \varsigma\mu\lambda^2/\delta - \mu\beta\lambda^2/\delta + 2\xi\lambda\mathrm{j}/\delta + 2\chi\varepsilon\xi\lambda\mathrm{j}/\delta$, $A_{hc} = \delta + 2\varepsilon\xi\lambda\mathrm{j}$,

$A_{ub} = 1 + \gamma + \delta - \mu\lambda^2 + 2\varepsilon\xi\lambda\mathrm{j} + 2\chi\varepsilon\xi\lambda\mathrm{j}$, $A_{hr} = \gamma + 2\varepsilon\xi\lambda\mathrm{j} + 2\chi\varepsilon\xi\lambda\mathrm{j}$.

When the suspension damping ratio ξ is set to 0.25, the maximum amplitude of the first dominant frequency in the amplitude-frequency characteristics of suspension dynamic deflection is M. If the HVRS stroke is L_h and the suspension stroke is Ls, then the percentage of HVRS stroke is $u_h = L_h/L_s$, and the maximum amplitude reached by the HVRS is $M_h = M(L_h/L_s)$. The probability of the HVRS working is *P(H)*.

If the amplitude of the deformation displacement of the HVRS is set as S_h, when $S_h \le M_h$, the HVRS is fully functional and the HVRS probability is 100%, which can be obtained as Equation (17). When $S_h > M_h$, the HVRS is not fully functional, and the probability of the HVRS working is as shown in Equation (18).

$$P(H) = 1 \qquad (S_h \le M_h) \tag{17}$$

$$P(H) = M_h/S_h \ \ (S_h > M_h) \tag{18}$$

The amplitude of sprung mass acceleration, relative dynamic load, dynamic deflection, equivalent inertial mass acceleration at any frequency point on the suspension amplitude-frequency characteristic curve is the sum of the amplitude with the HVRS multiplied by probability and the amplitude without the HVRS multiplied by probability,

The amplitude of various parameters such as sprung mass acceleration, relative dynamic load, dynamic deflection, shock absorber speed, equivalent inertial mass acceleration, and HVRS speed at any given frequency point on the suspension amplitude-frequency characteristic curve, is determined by the weighted sum of two scenarios: one with the influence of HVRS and the other without. The amplitudes in both cases are multiplied by their respective probabilities, which combined, form the overall response at that frequency, as shown in Equations (19)–(24).

$$|H_{hx}(\mathrm{j}\omega)|_{\ddot{z}_s\sim\dot{z}_r} = \omega\left|\frac{X_{z_{sh}}}{X_{z_{rh}}}\right|P(H) + \omega\left|\frac{X_{z_s}}{X_{z_r}}\right|(1 - P(H)) \tag{19}$$

$$\left|H_{hx}(\mathrm{j}\omega)_{(F_d/G_j)\sim\dot{z}_r}\right| = \left|\frac{\omega_{s0}(\gamma\omega_{s0}+2\varepsilon\xi\omega\mathrm{j})}{(1+\mu)g}\right|\left(\left|\frac{X_{F_{dh}}}{X_{z_{rh}}}\right|P(H)+\left|\frac{X_{F_d}}{X_{z_r}}\right|(1-P(H))\right) \tag{20}$$

$$|H_{hx}(\mathrm{j}\omega)|_{s_d\sim\dot{z}_r} = \frac{1}{\omega}\left|\frac{X_{s_{dh}}}{X_{z_{rh}}}\right|P(H)+\frac{1}{\omega}\left|\frac{X_{s_d}}{X_{z_r}}\right|(1-P(H)) \tag{21}$$

$$|H_{hx}(\mathrm{j}\omega)|_{v_{sh}\sim\dot{z}_r} = \left|\frac{X_{v_{sh}}}{X_{z_{rh}}}\right|P(H)+\left|\frac{X_{s_d}}{X_{z_r}}\right|(1-P(H)) \tag{22}$$

$$|H_{hx}(\mathrm{j}\omega)|_{a_{sh}\sim\dot{z}_r} = \omega\left|\frac{X_{v_{sh}}}{X_{z_{rh}}}\right|P(H)+\omega\left|\frac{X_{s_d}}{X_{z_r}}\right|(1-P(H)) \tag{23}$$

$$|H_{hx}(\mathrm{j}\omega)|_{v_{hu}\sim\dot{z}_r} = \left|\frac{X_{v_{hu}}}{X_{z_{rh}}}\right|P(H) \tag{24}$$

4.2. Frequency Domain Characteristics of the Electromechanical Suspension with an HVRS

The simulation parameters are shown in Tables 2 and 3. Equations (19)–(21) were calculated to obtain the amplitude-frequency characteristic curve of the suspension with an HVRS and compared with the characteristic curve of the traditional energy feedback suspension. The results are shown in Figure 6.

Table 3. Simulation parameters of HVRS suspension.

Parameter	Value	Parameter	Value
M	0.35	u_h	0.1
δ	1.5	χ	5
		ς	0.006

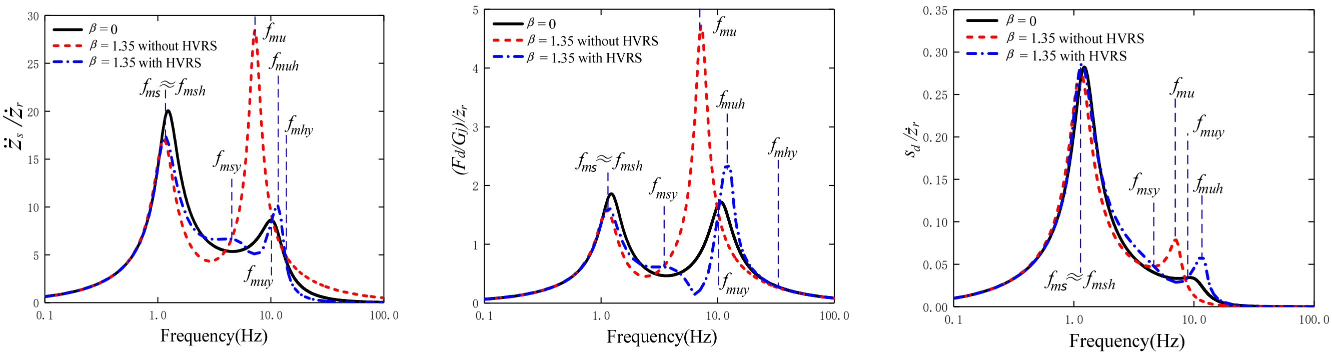

(**a**) (**b**) (**c**)

Figure 6. (**a**) Comparison of sprung mass acceleration amplitudes; (**b**) comparison of relative dynamic load amplitudes; (**c**) comparison of dynamic deflection amplitudes.

According to Equations (2), (3) and (23), we obtain the amplitude-frequency characteristic curve of the inertial force of the suspension with an HVRS and compare it with the inertial force characteristic curve of the traditional energy feedback suspension. The results are shown in Figure 7.

In Figure 6a–c, the first dominant frequency of suspension without an HVRS is f_{ms}, and the second main frequency is f_{mu}. The first dominant frequency of suspension with an HVRS is f_{msh}, and the second main frequency is f_{muh}. The intersection points of frequency domain characteristics between an HVRS suspension and a non-HVRS suspension, from low frequency to high frequency, are f_{msy}, f_{muy}, and f_{mhy}, respectively.

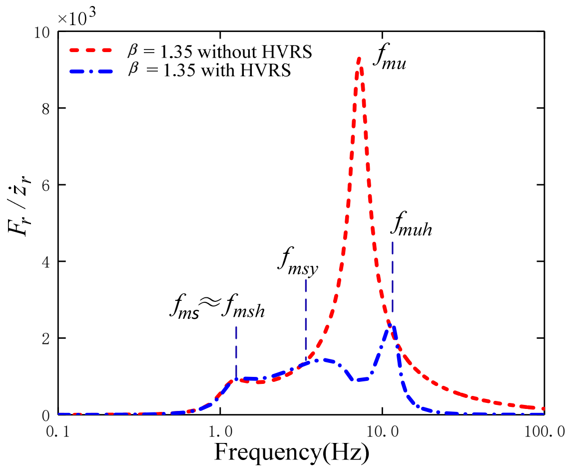

Figure 7. Comparison of inertial force amplitudes.

From Figure 6a, it can be seen that when the excitation frequency is lower than the frequency f_{msy}, the sprung mass acceleration of the HVRS suspension slightly increases compared to the original configuration suspension in the first main frequency range. When the excitation frequency is higher than the frequency f_{msy} but lower than the frequency f_{muy}, the sprung mass acceleration of HVRS suspension is significantly reduced compared to the original configuration suspension. When the excitation frequency is higher than the frequency f_{muy} but lower than the frequency f_{mhy}, the sprung mass acceleration of HVRS suspension slightly increases compared to the original configuration suspension. When the excitation frequency is higher than the frequency f_{mhy}, the sprung mass acceleration of HVRS suspension is significantly reduced compared to the original configuration suspension. It can be seen that HVRS suspension can solve the problem of deteriorating sprung mass acceleration caused by the equivalent inertial mass.

From Figure 6b, it can be seen that when the excitation frequency is lower than the frequency f_{msy}, the relative dynamic load of HVRS suspension slightly increases compared to the original configuration suspension in the first main frequency range. When the excitation frequency is higher than the frequency f_{msy} but lower than the frequency f_{muy}, the relative dynamic load of HVRS suspension is significantly reduced compared to the original configuration suspension. When the excitation frequency is higher than the frequency f_{muy} but lower than the frequency f_{mhy}, the relative dynamic load of the HVRS suspension increases in the second main frequency range. When the excitation frequency is higher than the frequency f_{mhy}, the relative dynamic load of HVRS suspension is essentially the same as the original configuration suspension. As for vehicle handling stability, the frequency of relative dynamic loads that it focuses on is generally less than 10 Hz, it can be seen that HVRS suspension can solve the problem of deteriorating vehicle handling stability caused by equivalent inertial mass.

Based on the analysis of Figure 6, the first main frequency f_{msh} of HVRS suspension is essentially the same as that of the original configuration suspension, and the second main frequency f_{muh} of HVRS suspension is greater than that of the original configuration suspension.

From Figure 7, it can be seen that the inertial force generated by the equivalent inertial mass of the energy regenerative suspension without an HVRS reaches its maximum at the second main frequency. By comparing Figure 7 with Figure 6a,b, it can be seen that the trend of inertial force variation of the energy regenerative suspension without an HVRS is the same as that of the acceleration of the sprung mass and the relative dynamic load variation. This is the reason why the acceleration of the sprung mass and the relative dynamic load deteriorate in the second main frequency region of the traditional configuration of energy regenerative suspension.

From Figure 7, it can be seen that the inertial force of the energy regenerative suspension with an HVRS is significantly reduced in the second main frequency amplitude, indicating that the HVRS can act as a low-pass filter. The HVRS essentially does not change the inertial force in the first main frequency range of the suspension but significantly reduces the inertial force in the second main frequency range, which can greatly improve suspension performance.

5. The Verification of HVRS Suspension Characteristics

5.1. Damping Force and Control of Energy-Regenerative Shock Absorber

There are two schemes for the damping control of energy-regenerative suspension. One is to adjust the damping coefficient by controlling the values of different dissipation resistances; the vibration energy of the suspension is ultimately dissipated through the heat generated by the resistance. The second is to adjust the damping coefficient by controlling the value of the recovered electrical energy, but the adjustment effect of the damping coefficient is related to the state of energy storage devices such as supercapacitors and batteries, and there are unstable factors. In order to study more accurately the beneficial effects of the new configuration on the energy feedback suspension, this paper adopts the scheme of controlling the dissipation resistance to achieve damping coefficient adjustment.

The damping control principle of the energy-regenerative shock absorber is shown in Figure 8. This paper adopts the mode of controlling electrical energy dissipation to control the load resistance R_r, thereby achieving the adjustment of damping force. The suspension controller sends a PWM control signal to the electronic switch Dr through the control line Cr, and the duty cycle of the PWM signal determines the conduction time of the load resistance R_r. The duty cycle of PWM is set to d_u, and the value range of du is from 0% to 100%. When $d_u = 0\%$, the load circuit of the energy feedback damper is equivalent to being disconnected, and the dissipation resistance R_d is infinite. When $d_u = 100\%$, the dissipation resistance of the energy regenerative damper is R_r. Therefore, the calculation formula for the dissipation resistance value R_d of the shock absorber under PWM control is Equation (25).

$$R_d = R_r/d_u \quad d_u \in (0,1] \tag{25}$$

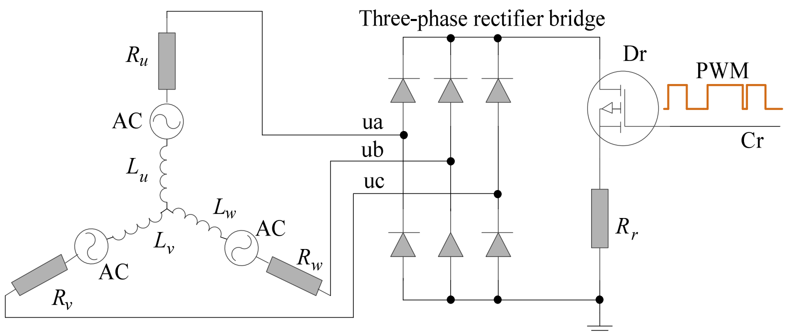

Figure 8. Damping control principle of energy-regenerative shock absorber.

According to paper [12,29,30], the damping coefficient of the energy-regenerative damper can be obtained as Equation (26), where k_e is the back electromotive voltage constant, k_t is the torque constant, and R_m is the internal resistance of the motor.

$$c_s = \frac{30k_e k_t i_r^2}{\pi r_g^2 (R_d + R_m)} \tag{26}$$

Using the parameters in Table 4, according to Equations (25) and (26), the variation curve of the dissipation resistance when the PWM duty cycle changes is shown in Figure 9a, and the variation curve of the suspension damping coefficient is shown in Figure 9b.

Table 4. Parameters of shock absorber.

Parameter	Symbol	Value	Unit
The back electromotive voltage constant	k_e	0.057	V/(r/min)
The torque constant	k_t	0.454	N·m/A
The internal resistance of the motor	R_m	1.1	Ω
The load resistance	R_r	20	Ω

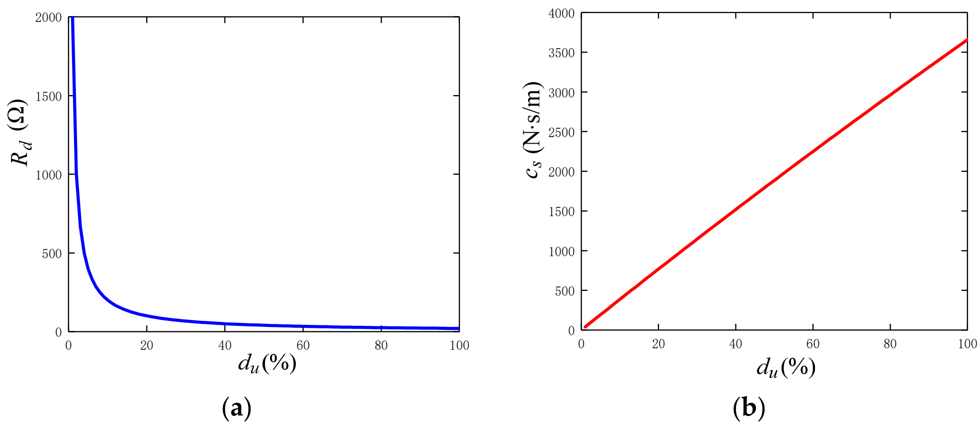

Figure 9. (**a**) The variation curve of dissipation resistance; (**b**) the variation curve of the suspension damping coefficient.

From Figure 9a, it can be seen that the PWM duty cycle d_u can adjust the dissipation resistance of the shock absorber, which is the basis for achieving semi-active suspension control. The variation of dissipation resistance is not linear with the variation of the PWM duty cycle. When the duty cycle is less than 20%, a small change in the duty cycle will cause a significant change in the dissipation resistance value.

From Figure 9b, it can be seen that the PWM duty cycle can adjust the damping coefficient of the suspension, and it essentially changes linearly, which is very beneficial for the control of the semi-active suspension. By adjusting the PWM duty cycle d_u, the damping coefficient can be quickly adjusted to the desired value.

5.2. Shock Absorber Structure with HVRS

To verify whether the suspension can overcome the adverse effects of equivalent inertial mass after adding an HVRS, an HVRS is added to the original shock absorber structure, as shown in Figure 10a. The HVRS is set between the planetary gearbox and the motor, with minimal structural changes to the original shock absorber, which is most conducive to implementation. On the other hand, due to the amplification effect of the transmission, the stiffness and damping of the HVRS are equivalent to the values in the suspension.

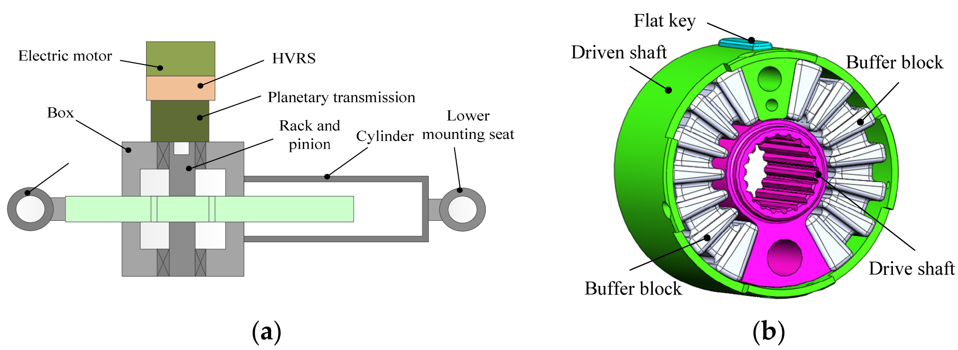

Figure 10. (**a**) Shock absorber structure with an HVRS; (**b**) the structure of the HVRS.

The structure of the HVRS is shown in Figure 10b; it is mainly composed of a drive shaft, a buffer block, a driven shaft, and a flat key. The driven shaft is connected to the motor rotor through a flat key; the driving shaft is connected to the transmission output shaft through splines. The material for the buffer block is wet-process rubber, which allows to achieve the elastic deformation and energy absorption functions of the HVRS, ensuring stiffness and service life requirements. It has a long-term temperature resistance of over 150 °C and a compressive strength of 27.8 MPa.

5.3. Quarter-Vehicle Test Setup

The structure of the suspension vibration test bench is shown in Figure 11.

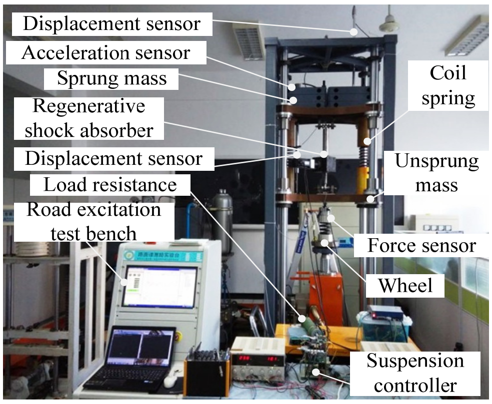

Figure 11. Quarter-vehicle test setup.

The road excitation test bench selects and controls the signals of the road excitation system, and its hydraulic actuator is located below the simulated wheel and generates simulated random road roughness, causing the suspension system to vibrate.

The quarter-vehicle suspension includes sprung mass, unsprung mass, suspension springs, a shock absorber, and a simulated wheel.

The displacement sensors, acceleration sensor, and force sensor arranged in the test bench collect state information during the vibration process of the suspension system and transmit it to the suspension control system. One of the displacement sensors is arranged between the unsprung mass and the sprung mass and is used to measure the dynamic deflection of the suspension. Another displacement sensor is arranged between the sprung mass and the test bench to measure the displacement of the sprung mass. The velocity signal of the sprung mass can be obtained by differentiating this signal. The accelerometer is arranged on the sprung mass to measure the acceleration of the sprung mass. The force sensor is arranged under the wheel to measure the dynamic load of the wheel during the test process.

The suspension controller calculates and processes the collected suspension status information based on the control strategy set by the upper computer, sends out PWM control signals to adjust the value of the dissipation resistance, and achieves semi-active control of the suspension.

5.4. Comparison of Vibration Shock Absorber Diagram

In order to compare the characteristics of two different shock absorbers, the dissipation resistor is configured as $R_d = 60\ \Omega$. Through a single degree of freedom test, the upper end of the shock absorber is fixed and a vertical sine signal with a frequency of 1 H and an amplitude of 50mm is input into the end of the shock absorber. The force–displacement curve and force–velocity curve with and without the HVRS are obtained as shown in Figure 12.

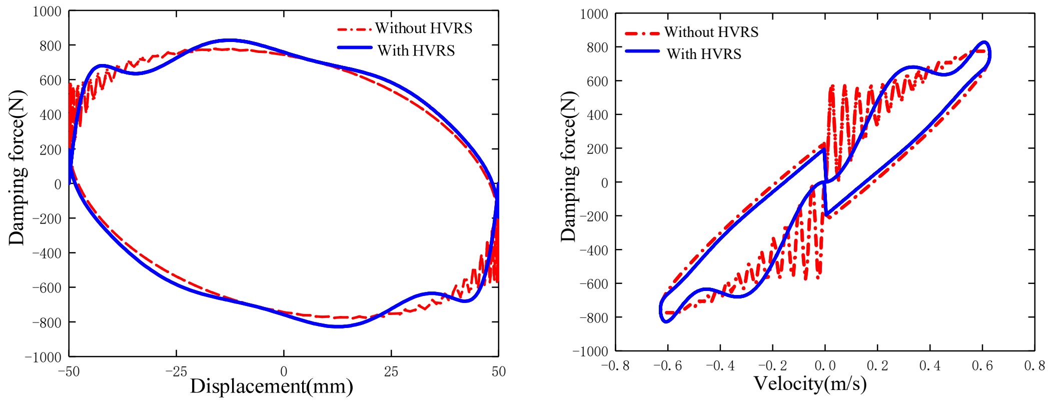

(**a**) (**b**)

Figure 12. (**a**) Damping force–displacement curve of shock absorber; (**b**) damping force–velocity curve of shock absorber.

Due to the presence of gaps in the meshing of gear and rack, when the shock absorber is reversing, it will produce an idle stroke. At this time, the equivalent inertial mass has a large acceleration, resulting in a large inertial force. The inertial force causes the damping force of the shock absorber to oscillate. From Figure 12, it can be seen that the shock absorber with an HVRS can eliminate the oscillation of the force curve compared to the shock absorber without an HVRS, making the damping force change of the force–displacement curve smooth, which is conducive to improving reliability and comfort.

From Figures 7 and 12, it can be seen that the HVRS does not attenuate inertial forces in the first main frequency region of the suspension, which is beneficial for suspension vibration reduction.

In order to further verify the attenuation effect of the HVRS on high-frequency inertial forces, the load resistance R_r in Figure 8 was disconnected. According to Equation (26), the damping coefficient of the suspension was essentially 0 at this time. Due to the fact that the damping force of the shock absorber was essentially 0, the shock absorber only output inertial force at that time. We input a vertical sine signal with a frequency of 10 H and an amplitude of 10 mm to the end of the shock absorber to obtain the inertial force–displacement curve and inertial force–velocity curve with and without the HVRS, as shown in Figure 13.

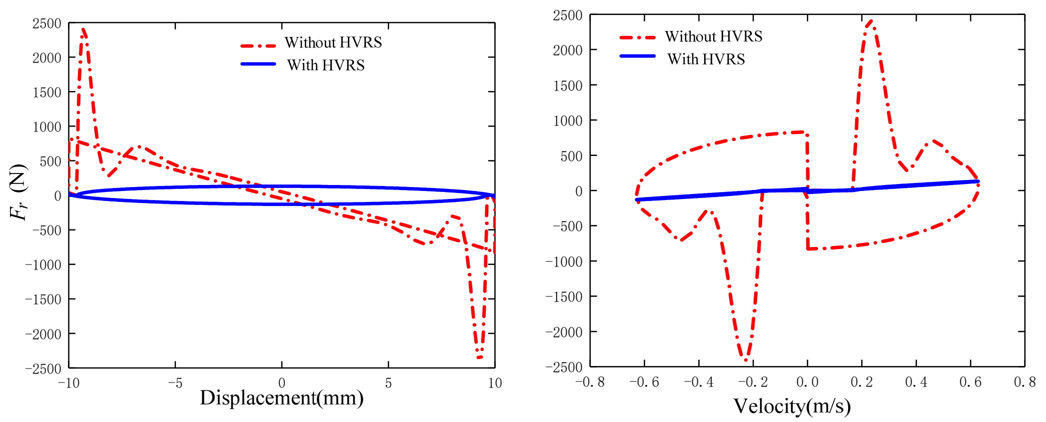

(**a**) (**b**)

Figure 13. (**a**) Inertial force–displacement curve of shock absorber; (**b**) inertial force–velocity curve of shock absorber.

From Figure 13, it can be seen that the inertial force curve of the damper without an HVRS shows oscillation, and the inertial force that is generated when the shock absorber changes direction is much greater than that of the shock absorber with an HVRS. The inertial force of the shock absorber with an HVRS is significantly attenuated.

From Figures 7 and 13, it can be seen that in the second and higher frequency regions of the suspension, the HVRS significantly reduces the inertial force, thereby improving the suspension performance.

It can be seen that the HVRS can not only eliminate the oscillation of the shock absorber force curve but also significantly attenuate the inertial force in the high-frequency region. From the perspective of energy recovery, after the application of the HVRS structure in the energy regenerative suspension, the recovered energy is mainly concentrated in the low-frequency region of suspension vibration, that is, the first main frequency region.

5.5. Random Road Comparison Test of Two Suspension Configurations

The parameters of the two suspension configurations in the bench comparison test are shown in Table 5. The road excitation for the suspension test is to use a standard C-class road surface at a speed of 60 km/h.

Table 5. Parameters of suspension.

Parameter	Symbol	Value	Unit
Sprung mass	m_s	312.5	kg
Unsprung mass	m_u	43.5	kg
Equivalent inertial mass	m_r	58.8	kg
Suspension spring stiffness	k_s	20,000	N/m
Wheel stiffness	k_u	180,000	N/m
Dissipation resistance	R_d	60	Ω
Suspension HVRS stiffness	k_h	30,000	N/m
Suspension HVRS damping coefficient	c_h	268	N·s/m

The time-domain data curves of the sprung mass acceleration $\sigma_{\ddot{z}_s}$, relative dynamic load σ_{F_d/G_j}, and dynamic deflection σ_{s_d} of two suspension configurations were obtained through experiments, as shown in Figure 14. The comparison of root mean square values of suspension characteristic data is shown in Table 6.

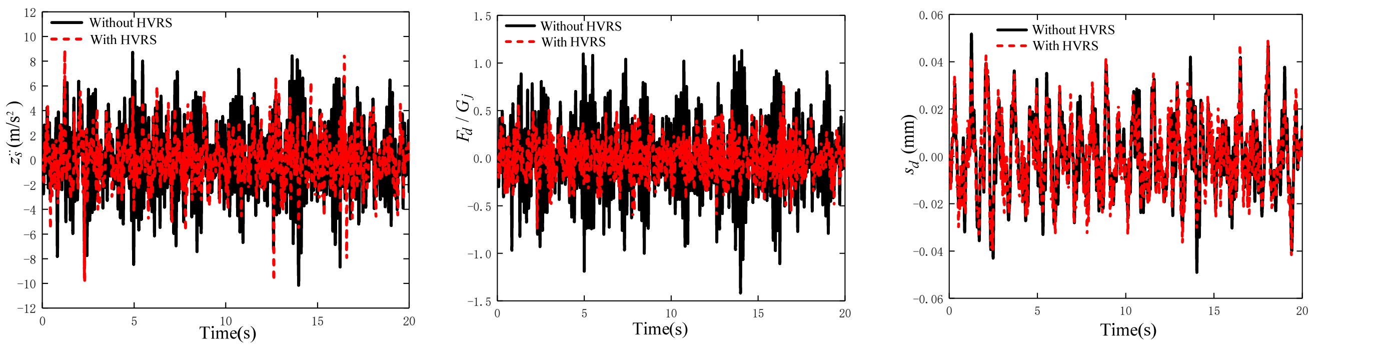

(**a**) (**b**) (**c**)

Figure 14. (**a**) Comparison of sprung mass acceleration; (**b**) comparison of relative dynamic loads; (**c**) comparison of dynamic deflection.

Table 6. Comparison of suspension test results.

Status	$\sigma_{\ddot{z}_s}$/m/s^2	σ_{F_d/G_j}	σ_{s_d}/m
Without HVRS	2.7963	0.3791	0.0161
With HVRS	1.8912	0.1936	0.0156
Changed	−32.37%	−48.93%	−3.11%

Analyzing Figure 14 and Table 6, it can be seen that the suspension characteristics of the two configurations are essentially the same in terms of dynamic deflection in the time domain. The root mean square value of dynamic deflection of HVRS suspension is 3.11% lower than that of suspension without an HVRS. the root mean square value of the sprung mass acceleration of HVRS suspension is 32.37% lower than that of suspension without an HVRS; the root mean square value of the relative dynamic load of HVRS suspension is 48.93% lower than that of suspension without an HVRS. Therefore, the HVRS is very effective in improving the performance of energy regenerative suspension.

To further analyze the reasons for the effectiveness of the HVRS from the frequency domain characteristics, the spectral density comparison of the suspension sprung mass acceleration, relative dynamic load, and dynamic deflection obtained through spectral analysis of experimental data is shown in Figure 15.

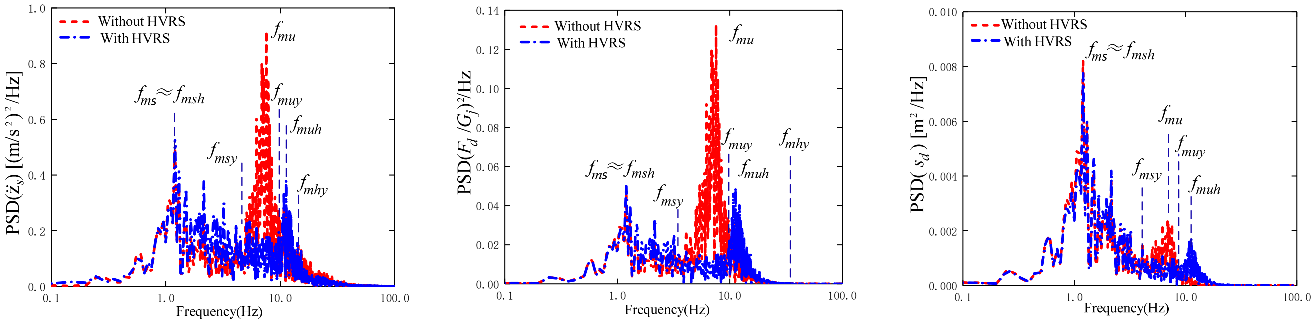

(**a**) (**b**) (**c**)

Figure 15. (**a**) Comparison of sprung mass acceleration spectral density; (**b**) comparison of relative dynamic load spectrum density; (**c**) comparison of dynamic deflection spectral density.

From Figure 15a, it can be seen that when the excitation frequency is lower than the frequency f_{msy}, the sprung mass acceleration of the HVRS suspension slightly increases compared to the original configuration suspension in the first main frequency range. When the excitation frequency is higher than the frequency f_{msy} but lower than the frequency f_{muy}, the sprung mass acceleration of HVRS suspension is significantly reduced compared to the original configuration suspension. When the excitation frequency is higher than the frequency f_{muy} but lower than the frequency f_{mhy}, the sprung mass acceleration of HVRS suspension slightly increases compared to the original configuration suspension. When the excitation frequency is higher than the frequency f_{mhy}, the sprung mass acceleration of HVRS suspension is significantly reduced compared to the original configuration suspension. It can be seen that HVRS suspension can solve the problem of deteriorating sprung mass acceleration caused by equivalent inertial mass.

From Figure 15b, it can be seen that when the excitation frequency is lower than the frequency f_{msy}, the relative dynamic load of HVRS suspension slightly increases compared to the original configuration suspension in the first main frequency range. When the excitation frequency is higher than the frequency f_{msy} but lower than the frequency f_{muy}, the relative dynamic load of HVRS suspension is significantly reduced compared to the original configuration suspension. When the excitation frequency is higher than the frequency f_{muy} but lower than the frequency f_{mhy}, the relative dynamic load of HVRS suspension increases in the second main frequency range. When the excitation frequency is higher than the frequency f_{mhy}, the relative dynamic load of HVRS suspension is essentially the same as the original configuration suspension. As for vehicle handling stability, as the frequency of relative dynamic loads that it focuses on is generally less than 10 Hz, it can be seen that HVRS suspension can solve the problem of deteriorating vehicle handling stability caused by equivalent inertial mass.

Based on the analysis of Figure 15, the first main frequency f_{msh} of HVRS suspension is essentially the same as that of the original configuration suspension, and the second main frequency f_{muh} of HVRS suspension is greater than that frequency f_{mu} of the original configuration suspension.

5.6. Semi-Active Control Test Verification

Due to the significant changes in the suspension configuration compared to traditional suspensions after the addition of an HVRS, it is necessary to verify whether the skyhook control algorithm is effective for HVRS suspensions. The skyhook control algorithm was first proposed by Karnopp et al. [31] and has been widely studied in academia and automotive industries as a means to improve ride comfort and road holding of vehicles with semi-active suspension.

To achieve semi-active control of the HVRS energy-regenerative suspension, the sprung mass speed v_s and the damper speed $(v_s - v_h)$ are selected as inputs for the skyhook control algorithm. The skyhook semi-active control algorithm for HVRS suspension is shown in Equation (27).

$$c_s = \begin{cases} c_{\text{sky}} v_s \,/ (v_s - v_h) \quad c_s \in (c_{\min}, c_{\max}]; & v_{\text{s}}(v_{\text{s}} - v_{\text{h}}) > 0 \\ c_{\min}; & v_{\text{s}}(v_{\text{s}} - v_{\text{h}}) \le 0 \end{cases} \tag{27}$$

Using the excitation signal of a vehicle traveling at a speed of 60 km/h on a C-level road surface as input, the semi-active control of HVRS suspension and the passive suspension state of the HVRS are compared and simulated, with a simulation duration of 20 s. The damping coefficient of passive suspension is constant. The time-domain data curves of the sprung mass acceleration, relative dynamic load, and dynamic deflection of two suspension configurations were obtained through experiments, as shown in Figure 16. For clearer comparison, only 5 s of data are shown in Figure 16. The comparison of root mean square values of suspension characteristic data is shown in Table 7.

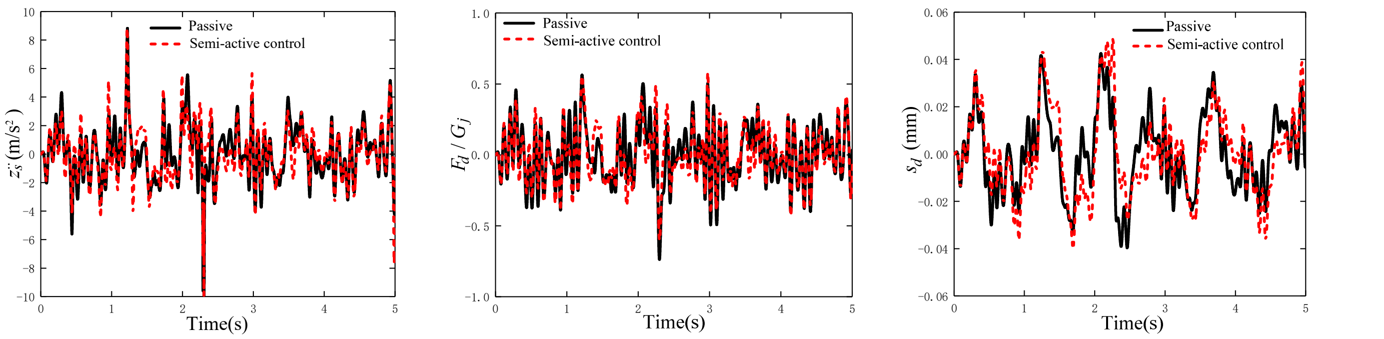

(**a**) (**b**) (**c**)

Figure 16. (**a**) Comparison of sprung mass acceleration; (**b**) comparison of relative dynamic loads; (**c**) comparison of dynamic deflection.

Table 7. Comparison of HVRS suspension test results.

Status	$\sigma_{\ddot{z}_s}$**/m/s²**	σ_{F_d/G_j}	σ_{s_d}**/m**
Passive HVRS	1.8912	0.1936	0.0156
Semi-active HVRS	1.7781	0.1796	0.0160
Changed	−5.98%	−7.23%	+2.56%

Through comparison, it can be seen that the semi-active control of HVRS suspension reduces the sprung mass acceleration by 5.98% compared to passive suspension, reduces the relative dynamic load by 7.23%, and increases the dynamic deflection by 2.56%. This indicates that the application of semi-active control algorithms in HVRS suspension can further improve performance while reducing the impact of equivalent inertial mass.

6. Conclusions

In order to solve the problems of performance degradation and low suspension reliability caused by the equivalent inertial mass of energy-regenerative suspension, this paper proposes an HVRS suspension configuration. Through frequency domain analysis and bench comparison experiments, it is proved that the new suspension configuration can improve the suspension performance. The following conclusions are drawn:

(1) Frequency domain analysis shows that an HVRS can significantly reduce the sprung mass acceleration and relative dynamic load of energy regenerative suspension.
(2) The suspension controller can achieve linear adjustment of the dissipation resistance value of the shock absorber through PWM control.
(3) An HVRS can not only eliminate the oscillation of the shock absorber force curve but also significantly attenuate the inertial force in the high-frequency region.
(4) The recovered energy regenerated by HVRS suspension is mainly concentrated in the first main frequency region of suspension vibration.
(5) By applying the skyhook semi-active control algorithm, the HVRS suspension can further reduce the sprung mass acceleration and relative dynamic load.

Author Contributions: Conceptualization, H.S. and M.D.; Methodology, H.S., M.D. and X.W.; Software, H.S., M.D. and X.W.; Validation, H.S., M.D. and X.W.; Formal analysis, H.S., M.D. and X.W.; Investigation, H.S., M.D. and X.W.; Resources, H.S.; Data curation, H.S., M.D. and X.W.; Writing—original draft preparation, H.S. and M.D.; Writing—review and editing, H.S., M.D. and X.W.; Visualization, M.D.; Supervision, H.S.; Project administration, H.S. All authors have read and agreed to the published version of the manuscript.

Funding: China National Basic Research Projects MKS20200006 and MKS20210070.

Institutional Review Board Statement: Not applicable.

Informed Consent Statement: Not applicable.

Data Availability Statement: Data are contained within the article.

Conflicts of Interest: The authors declare no conflicts of interest.

References

1. Karnopp, D. Permanent Magnet Linear Motors Used as Variable Mechanical Dampers for Vehicle Suspensions. *Veh. Syst. Dyn.* **1989**, *18*, 187–200. [CrossRef]
2. Jones, W.D. Easy ride: Bose Corp. uses speaker technology to give cars adaptive suspension. *IEEE Spectr.* **2005**, *42*, 12–14. [CrossRef]
3. Xuechun, Z.; Fan, Y.; Yongchao, Z. A Novel Energy-regenerative Active Suspension for Vehicles. *J. Shanghai Jiaotong Univ. Sci.* **2008**, *13*, 184–188.
4. Xiong, Q.; Qin, B.; Li, X.; Zuo, L. The Development of a Flexible Damping Tunning Rule-Based Control for MMR-Based Energy Harvesting Suspension. In Proceedings of the ASME 2020 American Control Conference ACC 2020-120, Denver, CO, USA, 1–3 July 2020.
5. Gao, Z.; Chen, S.; Zhao, Y.; Liu, Z. Numerical evaluation of compatibility between comfort and energy recovery based on energy flow mechanism inside electromagnetic active suspension. *Energy* **2019**, *170*, 521–536. [CrossRef]
6. Xiudong, T.; Teng, L.; Zuo, L. Design and Optimization of a Tubular Linear Electromagnetic Vibration Energy Harvester. *IEEE ASME Trans. Mechatron.* **2014**, *19*, 615–622.
7. Lee, J.; Chun, Y.; Kim, J.; Park, B. An Energy-Harvesting System Using MPPT at Shock Absorber for Electric Vehicles. *Energies* **2021**, *14*, 2552. [CrossRef]
8. Li, S.; Xu, J.; Pu, X.; Tao, T.; Gao, H.; Mei, X. Energy-harvesting variable/constant damping suspension system with motor based electromagnetic damper. *Energy* **2019**, *189*, 116199–116211. [CrossRef]
9. Hua, Y.; Cai, Q.; Zhu, S. Energy-Regenerative Semiactive Lateral Suspension Control in High-Speed Trains Using Electromagnetic Damper Cum Energy Harvester. *IEEE Trans. Veh. Technol.* **2022**, *71*, 4801–4812. [CrossRef]
10. Abdelkareem, M.A.A.; Lin, X.; Ahmed, A.M.K.; Elagouz, A.; Mi, J.; Guo, S.; Liu, Y.; Zuo, L. Vibration Energy Harvesting in Automotive Suspension System: A Detailed Review. *Appl. Energy* **2018**, *229*, 672–699. [CrossRef]
11. Zhang, J.-Q.; Peng, Z.-Z.; Yue, J.; Peng, Y.-M.; Wang, Z. Review of Regenerative Suspension Technology for Vehicle. *J. Acad. Armored Force Eng.* **2012**, *26*, 1–7.
12. Li, Z.; Zuo, L.; Luhrs, G.; Lin, L.; Qin, Y.-X. Electromagnetic Energy-Harvesting Shock Absorbers: Design, Modeling, and Road Tests. *IEEE Trans. Veh. Technol.* **2013**, *62*, 1065–1074. [CrossRef]

13. Liu, S.S.; Wang, Q.N.; Wang, W.H.; Lin, X. Influence of inertial mass on damping and amplitude-frequency characteristic of regenerative suspension. *J. Jilin Univ.* **2013**, *43*, 557–563.
14. Peng, H.; Zhang, J.; Wang, X.; Sun, Y.; Yao, J. Influence of Inertia Mass on Electromagnetic Suspension Damping and Amplitude Frequency Characteristics. In Proceedings of the International Symposium 2018, Hong Kong, 29–30 December 2018.
15. Yu, C.; Rakheja, S.; Wang, W.; Wang, Q. Analysis of an 'on-off' regenerative electromechanical damper. *Proc. Inst. Mech. Eng. Part D J. Automob. Eng.* **2013**, *227*, 704–722. [CrossRef]
16. Wang, Z.; Zhang, T.; Zhang, Z.; Yuan, Y.; Liu, Y. A high-efficiency regenerative shock absorber considering twin ball screws transmissions for application in range-extended electric vehicles. *Energy Built Environ.* **2020**, *1*, 36–49. [CrossRef]
17. Li, H.; Zheng, P.; Zhang, T.; Pan, Y.; Zhang, Z.; Azam, A. A high-efficiency energy regenerative shock absorber for powering auxiliary devices of new energy driverless buses. *Appl. Energy* **2021**, *295*, 117020. [CrossRef]
18. Liwei, D.; Fan, Y.; Ankang, H.; Guo, Z.; Yu, J.; Zuo, J. Investigation on energy-regenerative shock absorber with adjustable damping and power for freight wagons. *Energy Convers. Manag.* **2022**, *254*, 115228.
19. Zhihong, Z.; Yuliang, G.; Shian, C. Experimental research on PMSM ball screw actuator and structural design suggestion of featured active suspension. *IEEE Access* **2020**, *99*, 66163–66177.
20. Montazeri-Gh, M.; Kavianipour, O. Investigation of the passive electromagnetic damper. *ActaMechanica* **2012**, *223*, 2633–2646. [CrossRef]
21. Shian, C.; Xudong, J.; Ming, Y.; Jiang, S.-M.; Chen, J.; Wang, Y.-X. A dual vibration reduction structure-based self-powered active suspension system with PMSM-ball screw actuator via an improved H2/H∞ control. *Energy* **2021**, *201*, 117590.
22. Giuliani, F.; Bellani, G. Suspension for Wheeled Vehicle. Patent WO2015/155712A1, 15 October 2015.
23. Doetsch, H.-P. Self-Adjusting Hydraulic Shock Absorber. Patent US2980418A, 18 April 1961.
24. Lee, P.P. Shock Absorber with Gas Charged Return Spring. Patent EP0260968A2, 23 March 1988.
25. Marking, J. Shock Absorber with Positive and Negative Gas Spring Chambers. U.S. Patent 6,135,434, 24 October 2000.
26. Mikułowski, G.; Wiszowaty, R.; Holnicki-Szulc, J. Characterization of a piezoelectric valve for an adaptive pneumatic shock absorber. *Smart Mater. Struct.* **2013**, *22*, 125011. [CrossRef]
27. Martini, A.; Bellani, G.; Fragassa, C. Numerical Assessment of a New Hydro-Pneumatic Suspension System for Motorcycles. *Int. J. Automot. Mech. Eng.* **2018**, *15*, 5308–5325. [CrossRef]
28. Chen, J.; Wu, Y.; He, X.; Zhang, L.; Dong, S. Suspension parameter design of underframe equipment considering series stiffness of shock absorber. *Adv. Mech. Eng.* **2020**, *12*, 99–111. [CrossRef]
29. Zhu, S.; Shen, W.-A.; Xu, Y.-L. Linear electromagnetic devices for vibration damping and energy harvesting: Modeling and testing. *Eng. Struct.* **2012**, *34*, 198–212. [CrossRef]
30. Xie, L.; Li, J.; Cai, S.; Li, X. Electromagnetic Energy-Harvesting Damper with Multiple Independently Controlled Transducers: On-Demand Damping and Optimal Energy Regeneration. *IEEE ASME Trans. Mechatron.* **2017**, *22*, 2705–2713. [CrossRef]
31. Karnopp, D.; Crosby, M.; Harwood, R.A. Vibration Control Using Semi-Active Suspension Control. *J. Eng. Ind.* **1974**, *96*, 619–626. [CrossRef]